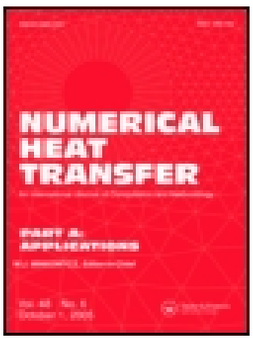

Numerical Heat Transfer, Part A: Applications

ISSN: 1040-7782 (Print) 1521-0634 (Online) Journal homepage: http://www.tandfonline.com/loi/unht20

MELT PRODUCTIVITY AND RHEOLOGY: COMPLEMENTARY INFLUENCES ON THE PROGRESS OF MELTING

S. A. Barboza & G. W. Bergantz

To cite this article: S. A. Barboza & G. W. Bergantz (1997) MELT PRODUCTIVITY AND RHEOLOGY: COMPLEMENTARY INFLUENCES ON THE PROGRESS OF MELTING, Numerical Heat Transfer, Part A: Applications, 31:4, 375-392, DOI: 10.1080/10407789708914043

To link to this article: http://dx.doi.org/10.1080/10407789708914043

Published online: 27 Apr 2007.

MELT PRODUCTIVITY AND RHEOLOGY: COMPLEMENTARY INFLUENCES ON THE PROGRESS OF MELTING

S. A. Barboza and G. W. Bergantz
Department of Geological Sciences, University of Washington, Box 351310, Seattle, Washington 98159, USA

The binary-eutectic model of phase change limits the application of continuum-mixture simulations to particular systems. We present a phase-change model that allows systems with more complex phase relations to be addressed. The model includes multiple invariant points, which yield a nonlinear production of melt as a function of temperature. A constitutive relation based on the hybrid model for viscosity and permeability is used to account for transport behavior as a function of the local melt fraction. Results are reported of two series of simulations, one utilizing the new two-invariant-point model and the other using a one-invariant-point model. The comparison demonstrates that the efficiency of convective heat transport can be increased by over 200% in the two-invariant-point case. The total kinetic energy for the two-invariant-point system is typically 2 orders of magnitude greater. This comparison highlights the important link between melt productivity and the constitutive relations and illustrates the necessity of accurately modeling the variation of melt fraction with temperature in partially molten systems.

INTRODUCTION

The equations governing the transport of heat and mass in solid-liquid phase-change systems require thermodynamic functions that link the enthalpy and mixture composition to the local melt fraction [1]. Previous studies have utilized a binary-eutectic phase diagram with a single invariant point and solid solution between the components of the system to provide the necessary equations [2–4]. However, the phase-change systematics of naturally occurring rock compositions are typically more complex. As an example, experimental studies have shown that, as long as feldspar (a tectosilicate) is not a limiting reactant, some rock compositions may exhibit large increases in melt fraction with increasing temperature as the solidi of the phyllosilicates are exceeded [5]. This nonlinear melt production may have a significant influence on heat and mass transfer, as the constitutive

Received 25 June 1996; accepted 11 October 1996.

Partial funding for this work was provided by NSF Grant EAR-9508291 and an AWU Faculty Fellowship to Battelle, Pacific Northwest Laboratory.

The authors acknowledge Jun Ni and Alberto Patiño Douce for fruitful discussions and assistance with numerical aspects, development of the governing equations, and derivation of the projected phase relations. The editorial assistance of Dr. W. J. Minkowycz and the helpful comments of two anonymous reviewers are also acknowledged.

Address correspondence to Professor George W. Bergantz, Department of Geological Sciences, University of Washington, Box 351310, Seattle, WA 98195-1310, USA. E-mail: bergantz@u.washington.edu

Numerical Heat Transfer, Part A, 31:375–392, 1997

1040–7782/97 $12.00 + .00

NOMENCLATURE

c_p^a	heat capacity at constant pressure of constituent a, J/kg K	β_T^a	coefficient of thermal expansion of constituent a, 1/K
C, C^a	solute concentration in the mixture and in constituent a, respectively, dimensionless	γ^a	mass of constituent a per unit volume of constituent a, kg/m^3
D^a	diffusion coefficient of constituent a, m^2/s	Γ	permeability switching function, dimensionless
f^a	mass fraction of constituent a, dimensionless	ϑ	flux ratio, dimensionless
g^a	volume fraction of constituent a, dimensionless	μ, μ^a	mixture viscosity and viscosity of constituent a, respectively, Pa s
g_i	ith component of gravitational acceleration, m/s^2	ρ	mass of mixture per unit volume of the mixture, kg/m^3
k	thermal conductivity, J/(s m K)	ρ^a	mass of constituent a per unit volume of the mixture, kg/m^3
K_i	ith component of anisotropic permeability, m^2	Φ	viscosity switching function, dimensionless
L	specific latent heat, J/K		
p	static pressure or isotropic stress of the mixture, Pa	**Subscript**	
t	time, s		
T	temperature, °C	0	reference value
v_i^a	ith component of mixture velocity of constituent a, m/s	**Superscripts**	
V_i	ith partial volume of the computational domain, m^3		
β_C^a	coefficient of solutal expansion of constituent a, 1/K	l	liquid phase
		s	solid phase

equations for the mixture depend explicitly on the melt fraction. However, the effect of the interdependence of melt production and the constitutive equations on heat and mass transfer is poorly understood.

We present a continuum-mixture model for binary systems with two invariant points—a eutectic and a peritectic. Notable features of the numerical study include variable viscosity, rheological switching functions, and melting of a natural rock composition. The example simulations illustrate that the dynamics of heat and mass transport in systems with multiple invariant points differ significantly from that of binary-eutectic systems. Caution is thus urged in applying the results of continuum simulations utilizing binary-eutectic phase-change models to systems with more complex phase relations.

CONTINUUM MODEL

This study adopts the two-phase mixture formulation developed by Bennon and Incropera [1]. The interested reader is directed to Prakash and Voller [3] and Bennon and Incropera [1] for a complete derivation and a discussion of the model assumptions. We include additional terms in the governing equations that account

for the variation of mixture viscosity as a function of temperature, concentration, and solid fraction. Only the final form of the dimensional equations is presented here. The variable-viscosity forms of the mixture continuum-conservation equations for phase change and convection in two dimensions are

$$\frac{\partial v_j}{\partial x_j} = 0 \tag{1}$$

$$\frac{\partial}{\partial t}(\rho v_i) + \frac{\partial}{\partial x_j}(\rho v_j v_i) = -\frac{\partial p}{\partial x_i} + \frac{\partial}{\partial x_j}\left(\mu^l \frac{\rho}{\rho^l}\frac{\partial v_i}{\partial x_j}\right) + \frac{\rho}{\rho^l}\frac{\partial v_i}{\partial x_j}\frac{\partial \mu^l}{\partial x_j}$$

$$+ g^l \gamma_0^l g_i\left[\beta_T^l (T - T_0) + \beta_C^l (C^l - C_0^l)\right] - \frac{\mu^l}{K_i}(f^l v_i^l) \tag{2}$$

$$\frac{\partial}{\partial t}(\rho T) + \frac{\partial}{\partial x_i}(\rho v_i T) = \frac{\partial}{\partial x_i}\left(\frac{k}{c_p^l}\frac{\partial T}{\partial x_i}\right) - \rho\frac{L}{c_p^l}\frac{\partial f^l}{\partial t} + \rho\frac{\left(c_p^l - c_p^s\right)}{c_p^l}\frac{\partial}{\partial t}(f^s T) \tag{3}$$

$$\frac{\partial}{\partial t}(\rho C) + \frac{\partial}{\partial x_i}(\rho v_i C) = \frac{\partial}{\partial x_i}\left(\rho f^l D^l \frac{\partial C}{\partial x_i}\right) + \frac{\partial}{\partial x_i}\left[\rho f^l D^l \frac{\partial}{\partial x_i}(C^l - C)\right]$$

$$- \frac{\partial}{\partial x_i}\left[\rho v_i (C^l - C)\right] \tag{4}$$

The influence of the microscopic geometry on macroscopic transport is modeled by semi-empirical source terms incorporated with the governing equations. For example, the last term on the right-hand side of the momentum conservation expression, Eq. (2), accounts for the viscous forces exerted by the solid phase on the percolating interstitial fluid. The mixture pressure is defined so as to include only the pressure changes that result from the impetus to fluid motion caused by the body force and dilatation due to relative motion between the mixture constituents. The hydrostatic contribution to pressure is incorporated with the buoyancy source term, which accounts for the density variations with temperature and composition gradients. The magnitudes of these density changes are given by the size of the thermal (β_T^l) and compositional (β_C^l) expansion coefficients. The method used in determining these coefficients is discussed by Barboza and Bergantz [6].

The source terms that appear in the energy and solute conservation expressions, Eqs. (3) and (4), account for the enthalpy to temperature relations and the difference between the diffusion of components through the solid and the liquid, respectively. Compositional diffusion in the solid is taken to be neglible relative to

that in the liquid in this analysis. A complete derivation of all of the governing equations and source terms is given by Prakash and Voller [3] and Bennon and Incropera [1].

In this model formulation, many of the source terms and variables are, themselves, a function of the local melt fraction. However, there is no universal agreement on the most appropriate constitutive relations that span the full range of melt fraction [7]. At low melt fraction, the melt flows within a rigid solid matrix whose velocity is either fixed (static phase change) or prescribed to be that of free body translation (continuous phase change) [1]. At high melt fraction, bulk viscous flow of the mixture occurs, and there is no relative motion between the melt and the suspended solids. We use the model of Oldenburg and Spera [4], in which arctangent switching functions are employed to shift between the end-member constitutive relations at a stipulated critical melt fraction (CMF). An illustration of this rheological model is shown in Figure 1.

This study assumes the CMF is an abrupt transition in the rheology of the system. At low melt fraction the rheology is that of a static solid with a percolating interstitial melt, while above the CMF it is of a fluid with suspended solids. Several studies have indicated a CMF of approximately 0.5 for some silicate systems [8, 9]. However, it is important to acknowledge recent experiments, which indicate that the notion of a distinct CMF requires substantial revision for geological systems undergoing partial melting [10, 11]. Barboza and Bergantz [6] adopted a ramped switching function, where the transition between the end-member transport types was initiated at the CMF to recognize these results. This approach is not adopted here because an abrupt rheological transition better illustrates the influence of the thermodynamics of phase change on the dynamics of the system.

The rheological switching functions are incorporated directly into the relations for permeability and the mixture viscosity. The permeability is related to the local melt fraction by the Blake-Kozeny-Carman equation [12]. The melt viscosity is calculated by the Shaw model [13], and the influence of suspensions is modeled by the Krieger and Dougherty relation [14]. The permeability and viscosity relations

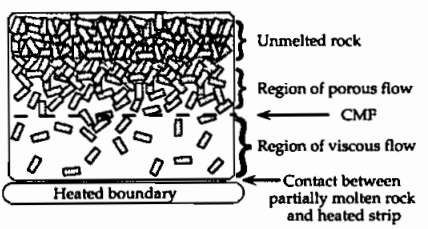

Figure 1. Schematic diagram of the rheological model. The base of a sequence of metasedimentary rocks is held at a constant temperature. Heat transfer to the sequence initiates partial melting and gives rise to double-diffusive convection of the mixture. Where the fraction of melt exceeds the critical melt fraction (CMF), bulk viscous flow of the partially molten mixture occurs. The suspended solids increase the bulk-mixture viscosity. Where the fraction of melt is less than the CMF, the solid is assumed to form a static-rigid matrix through which the melt flows.

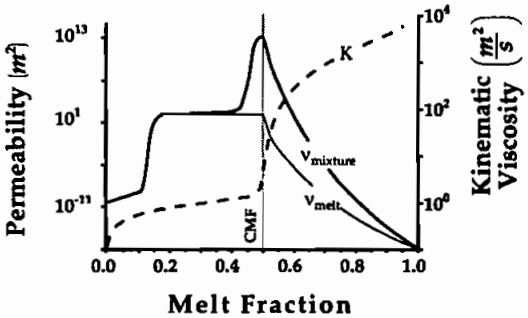

Figure 2. Plot of the kinematic viscosity of the mixture (heavy solid line) and the melt (thin solid line). The permeability (dashed line) is also shown. For $f^l > 0.5$ the switching function ensures that viscous drag between the mixture constituents is negligible relative to the body force. The influence of suspensions in the melt on the mixture viscosity is modeled by the Krieger and Dougherty relation [14]. For $f^l < 0.5$ the permeability is related to the porosity by the Blake-Kozeny-Carman equation [12], and the mixture viscosity is that of the melt as calculated by the Shaw model [13].

along with their associated switching functions are

$$K = \Gamma K_0 \left(\frac{(f^l)^3}{(1 - f^l)^2} \right) \tag{5}$$

$$\Gamma = \left(0.5 + \frac{1}{\pi} \arctan\left[100(f^l_{\text{crit}} - f^l) \right] \right)^{-10} \tag{6}$$

$$\mu(T, C, f^l) = \left[1 - \Phi \left(\frac{1 - f^l}{f^l_{\text{crit}}} \right) \right]^{-2} \mu^l(T, C) \tag{7}$$

$$\Phi = 0.5 - \frac{1}{\pi} \arctan\left[100(f^l_{\text{crit}} - f^l) \right] \tag{8}$$

The model rheological functions are illustrated in Figure 2.

PHASE DIAGRAM

The material chosen for the example calculations is a natural metasedimentary rock composition rich in phyllosilicate minerals (metapelite) whose predominant major element composition is within the system KFMASH (SiO_2-Al_2O_3-MgO-FeO-K_2O-H_2O). The exact composition and mineralogy are described by

Vielzeuf and Holloway [5]. A metapelite was chosen because of its importance in the earth sciences as a potential source of granitic melt [15]. One notable melting feature of this pelite composition is that it exhibits large jumps in melt fraction at two invariant points. The phase relations were experimentally derived by Patiño Douce and Johnston [16] using their own data along with those of Vielzeuf and Holloway [5] and Le Breton and Thompson [17].

The temperatures and compositions of the melts produced in the experiments and the deduced invariant points were projected onto a pseudobinary to derive the model binary phase diagram. The justification, methodology, and assumptions involved in making this projection are provided elsewhere [6, 18]. One should note, however, that the following two-invariant-point phase diagram is easily adapted to any two-invariant-point binary system. Some important geological examples include the systems Mg_2SiO_4-SiO_2 (forsterite-silica), $KAlSi_2O_6$-SiO_2 (leucite-silica), and $NaAlSiO_4$-$NaAlSi_3O_8$ (nepheline-albite).

Closure of the governing equations requires additional relations that link the mixture enthalpy and composition to the melt fraction [1]. This information is obtained by assuming local thermodynamic equilibrium and consulting the phase diagram. Note that macroscopic disequilibrium is not precluded even though local equilibrium is assumed. The procedure for deriving the lever-rule expressions for binary-eutectic systems has been discussed elsewhere [3]. However, numerous additional mathematical relations are required owing to the additional complexity with the presence of a second invariant point (the peritectic). Our approach was to divide the temperature-composition (T-X) space of the phase diagram into regions. The numbered regions are illustrated on the schematic of the two-invariant-point binary shown in Figure 3. The associated terminology and equilibrium lever-rule expressions are listed in Table 1, and Table 2 lists the values of the various constants. Separate univariant (solidus and liquidus) lines with different slopes were assigned to each T-X region. For example, in Figure 3, *Tlqs* the liquidus curve in region 5.

The parameters required to fix the geometry of the regions were obtained by fitting the experimental variation of melt fraction with temperature [5] to that predicted by the model. The fit between the model predictions and the experimental observations is illustrated in Figure 4. Although the geometry of this model is considerably more complex than that of previous phase diagrams, we attempted to maintain consistency with previously used terminology as much as possible [3]. Note, however, that much of the adopted terminology no longer has a meaningful physical interpretation and the constants should be regarded only as geometric parameters that define the position of the phase diagram in T-X space.

One complication with this approach is the thermodynamics of the system at the invariant points. Specifically, accounting for the transport of heat in phase-change systems requires careful consideration of the consumption or release of latent heat. However, stipulating a constant temperature and accounting for the latent heat exchange at the invariant points renders a discontinuity in the temperature field and results in difficult numerical instabilities. Our solution was to allow the system to change a few degrees in temperature during invariant-point phase change (Figure 3). This permits the use of lever-rule-type expressions to account for the variation of melt fraction with enthalpy exchange. This approach properly

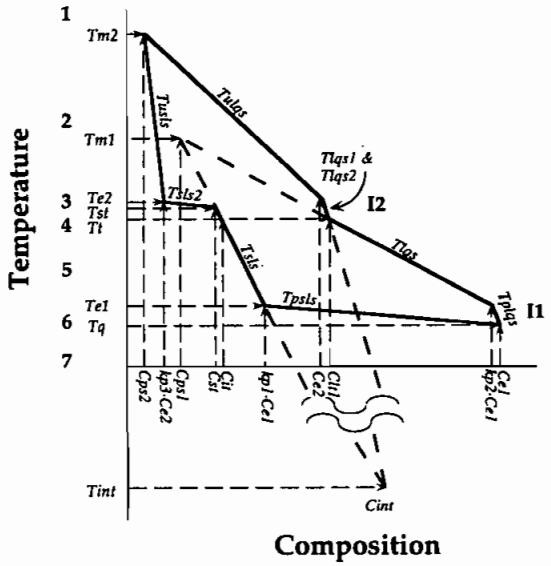

Figure 3. Schematic of the two-invariant-point binary phase diagram. The parameters in italics listed along the temperature and composition axis fix the geometry of the univariant lines in temperature-composition (*T-X*) space. The values of these parameters are either constant (Table 2) or prescribed by linking functions (Table 1). The linking functions ensure that there is a smooth transition between univariant lines in each of the *T-X* regions. The *T-X* regions are defined by the intervals between the temperature parameters and are indicated by the numbers printed in bold along the temperature axis. These numbers correspond to the *T-X* regions listed in Table 1. I1 and I2 indicate the eutectic and peritectic, respectively. The formulae specifying the slope of the univariant lines (*Tlqs*, *Tsls*, etc.) ae given in Table 1.

accounts for the latent heat of fusion, yet prevents discontinuities in the temperature field. An illustration of the geometry of the phase diagram in the vicinity of the eutectic and peritectic (I1 and I2) is shown in Figure 3.

Care must also be taken to ensure a smooth transition between each of the univariant lines for the separate regions. Discontinuities in any of the liquidus or solidus lines for the overall phase diagram will result in numerical instabilities and difficulty in obtaining a converged solution. In other words, the univariant lines for adjacent regions must precisely intersect at the prescribed temperature and composition where the transition between the *T-X* regions occurs. Expressions are therefore required to link the univariant lines from the different regions. The required expressions for the model phase diagram are provided in Table 1.

Table 1*a*. Geometry of phase diagram

Region	Slope of liquidus	Slope of solidus	Temperature range	Notes
1	na	na	$T > Tm2$	above the liquidus for all *Cmix*
2	$Tulqs = Tm2 + (Te2 - Tm2)\left(\frac{Cmix - Cps2}{Ce2 - Cps2}\right)$	$Tusls = Tm2 + (Te2 - Tm2)\left(\frac{Cmix - Cps2}{kp3 \cdot Ce2 - Cps2}\right)$	$Tm2 \geqslant T > Te2$	
3	$Tlqs2 = Te2 + (Tt - Te2)\left(\frac{Cmix - Ce2}{Clt1 - Ce2}\right)$	$Tsls2 = Te2 + (Tt - Te2)\left(\frac{Cmix - kp3 \cdot Ce2}{Clt1 - kp3 \cdot Ce2}\right)$	$Te2 \geqslant T > Tst$	peritectic region
4	$Tlqs1 = Te2 + (Tt - Te2)\left(\frac{Cmix - Ce2}{Clt1 - Ce2}\right)$	$Tsls1 = Tm1 + (Te1 - Tm1)\left(\frac{Cmix - Cps1}{kp1 \cdot Ce1 - Cps1}\right)$	$Tst \geqslant T > Tt$	peritectic region
5	$Tlqs = Tm1 + (Te1 - Tm1)\left(\frac{Cmix - Cps1}{kp2 \cdot Ce1 - Cps1}\right)$	$Tsls = Tm1 + (Te1 - Tm1)\left(\frac{Cmix - Cps1}{kp1 \cdot Ce1 - Cps1}\right)$	$Tt \geqslant T > Te1$	
6	$Tplqs = Te1 + (Tq - Te1)\left(\frac{Cmix - kp2 \cdot Ce1}{Ce1 - kp2 \cdot Ce1}\right)$	$Tpsls = Tq + (Te1 - Tq)\left(\frac{Cmix - Ce1}{kp1 \cdot Ce1 - Ce1}\right)$	$Te1 \geqslant T \geqslant Tq$	eutectic region
7	na	na	$T > Tq$	below the solidus for all *Cmix*

Table 1*b*. Melt fractions and phase compositions

Region	Melt fraction	Liquid composition	Solid composition
1	$f^l = 1$	$Cliq = Cmix$	na
2	$f^l = \left[\frac{1}{1-\left(\frac{kp3\cdot Ce2 - Cps2}{Ce2 - Cps2}\right)}\right]\left[\frac{T - Tulqs}{T - Tm2}\right]$	$Cliq = \left(\frac{f^l - 1}{f^l_{max4} - 1}\right)(Ce2 - Cmix) + Cmix$	$Csol = \left(\frac{f^l - 1}{f^l_{max4} - 1}\right)(kp3\cdot Ce2 - Cmins) + Cmix$
3	$f^l = \left[\frac{1}{1-\left(\frac{kp4 - 1}{kp3 - 1}\right)}\right]\left[\frac{T - Tsls2}{T - Tt}\right]$	$Cliq = \left(\frac{f^l - f^l_{max4}}{f^l_{max3} - f^l_{max4}}\right)(Clt2 - Ce2) + Ce2$	$Csol = \left(\frac{f^l - f^l_{max4}}{f^l_{max3} - f^l_{max4}}\right)(Cst - kp3\cdot Ce2) + kp3\cdot Ce2$
4	$f^l = \left[\frac{1}{1-\left(\frac{kint2 - 1}{kint1 - 1}\right)}\right]\left[\frac{T - Tsls1}{T - Tint}\right]$	$Cliq = \left(\frac{f^l - f^l_{max3}}{f^l_{max2} - f^l_{max3}}\right)(Clt1 - Clt2) + Clt2$	$Csol = \left(\frac{f^l - f^l_{max3}}{f^l_{max2} - f^l_{max3}}\right)(Cit - Cst) + Cst$
5	$f^l = 1 - \left[\frac{1}{1-\left(\frac{kp1\cdot Ce1 - Cps1}{kp2\cdot Ce1 - Cps1}\right)}\right]\left[\frac{T - Tlqs}{T - Tm1}\right]$	$Cliq = \left(\frac{f^l - f^l_{max2}}{f^l_{max1} - f^l_{max2}}\right)(kp2\cdot Ce1 - Clt1) + Clt1$	$Csol = \left(\frac{f^l - f^l_{max2}}{f^l_{max1} - f^l_{max2}}\right)(kp1\cdot Ce1 - Cit) + Cit$
6	$f^l = \left[\frac{1}{1-\left(\frac{kp2 - 1}{kp1 - 1}\right)}\right]\left[\frac{T - Tpsls}{T - Tq}\right]$	$Cliq = \left(1 - \frac{f^l}{f^l_{max1}}\right)(Ce1 - kp2\cdot Ce1) + kp2\cdot Ce1$	$Csol = \left(1 - \frac{f^l}{f^l_{max1}}\right)(Cmix - kp1\cdot Ce4) + kp1\cdot Ce1$
7	$f^l = 0$	na	$Csol = Cmix$

Table 1c. Auxiliary relations and linking functions

$$f^{l}_{max1} = \frac{Cmix - kp1 \cdot Ce1}{kp2 \cdot Ce1 - kp1 \cdot Ce1}$$

$$f^{l}_{max2} = \frac{Cmix - Cit}{Clt1 - Cit}$$

$$f^{l}_{max3} = \frac{Cmix - Cst}{Clt2 - Cst}$$

$$f^{l}_{max4} = \frac{Cmix - kp3 \cdot Ce2}{Ce2 - kp3 \cdot Ce2}$$

$$Cmins = Cps2 + (kp3 \cdot Ce2 - Cps2)\left(\frac{Tulqs - Tm2}{Te2 - Tm2}\right)$$

$$Tint = \frac{Cps1 - Ce2 + Te2\left(\frac{Clt1 - Ce2}{Tt - Te2}\right) - Tm1\left(\frac{kp1 \cdot Ce1 - Cps1}{Te1 - Tm1}\right)}{\left(\frac{Clt1 - Ce2}{Tt - Te2}\right) - \left(\frac{kp1 \cdot Ce1 - Cps1}{Te1 - Tm1}\right)}$$

$$Cint = Ce2 + (Clt1 - Ce2)\left(\frac{Tint - Te2}{Tt - Te2}\right)$$

$$Kint1 = \frac{Cst}{Cint}$$

$$Kint2 = \frac{Clt2}{Cint}$$

$$Cit = Cps1 + (kp1 \cdot Ce1 - Cps1)\left(\frac{Tt - Te2}{Cps1 - kp3 \cdot Ce2}\right)$$

$$Cst = kp3 \cdot Ce2 + (Clt1 - kp3 \cdot Ce2)\left(\frac{Tst - Te2}{Tt - Te2}\right)$$

$$Tst = \left(\frac{B}{Tt - Te2}\right) - A$$

$$A = (Te1 - Tm1)[Te2(Clt1 - kp3 \cdot Ce2) + (Tt - Te2)](Cps1 - kp3 \cdot Ce2)$$

$$B = Tm1(Tt - Te2)kp1 \cdot Ce1 - A$$

$$Clt1 = Cps1 + (kp2 \cdot Ce1 - Cps1)\left(\frac{Tt - Tm1}{Te1 - Tm1}\right)$$

$$Clt2 = Ce2 + (Clt1 - Ce2)\left(\frac{Tst - Te2}{Tt - Te1}\right)$$

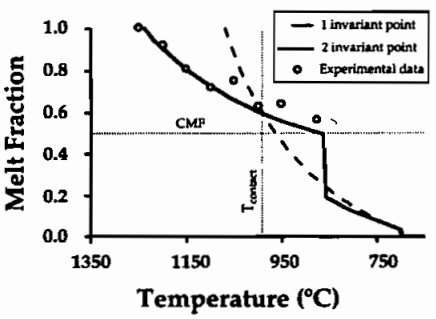

Figure 4. Plot of the melt productivity for both invariant-point cases. Solid line illustrates the variation of melt fraction with temperature of the two-invariant-point system, and the dashed line is that of the one-invariant-point system. The circles are the experimental data used to derive the geometry of the two-invariant-point phase diagram. The melt productivity of the one-invariant-point system was constructed so that both systems had the same melt fraction at the contact temperature ($T_{contact}$).

NUMERICAL SOLUTION

The governing equations, Eqs. (1)–(4), are in a form similar to the standard governing equations for single-phase systems, and any established numerical procedure may be employed to solve them. The methodology used in this study is that of the control volume formulation [19]. The PHOENICS algorithm [20] was employed to carry out the solution of the governing equations, and the mass fractions were updated iteratively, following the procedures outlined by Prakash and Voller [3]. Details of the numerical procedures and aspects of the particular application of the PHOENICS algorithm have been provided elsewhere [3, 18]. The major differences between the previous studies and this one are that this study includes (1) temperature, composition, and melt fraction dependent viscosity; (2) a new two-invariant-point phase diagram; (3) more precise accounting for enthalpy exchange at the invariant points; (4) switching functions for the permeability and viscosity following Oldenburg and Spera [4]; (5) melting from below, rather than solidification from the side; and (6) melting of a natural rock composition.

EXAMPLE PROBLEM

We consider the progress of melting of a sequence of metapelitic rocks in a two-dimensional, 200 m × 200 m computational domain heated from below (Figure 5). This configuration was chosen because it is suspected to be important in the generation of some classes of igneous rocks [15]. The results are then compared with the melting of a hypothetical material that possesses identical thermophysical properties but whose melting relations are best characterized by a binary eutectic. The equilibrium melt fraction versus temperature curves for the pelite and the hypothetical binary material are shown in Figure 4. The heated strip was 100 m in width and long enough that the important features of the convection could be captured in two dimensions. The computational domain was oriented such that the right wall was normal to, and intersected the center of the heated strip (Figure 5). A 60 × 60 graded grid, slightly biased in both dimensions toward the heated strip, was employed. A grid refinement study was undertaken to ensure that the solutions were independent of spatial and temporal discretization.

The simulations used a set of conditions characteristic of the melting of crustal rock in analogous geological systems. Justification for these conditions is

provided by Barboza and and Bergantz [6]. At time $t = 0$ the temperature along the heated strip was elevated to a value of T_{contact}. This contact temperature was maintained throughout the duration of the simulations. All other boundaries are thermally insulated. No-slip boundary conditions were employed on the left wall, roof, and floor, and free-slip conditions were proscribed on the right wall. A summary of the various model parameters used in the simulations is given in Table 2 and Figure 5.

Bennon and Incropera [2] and Oldenburg and Spera [21] have argued cogently that the variable composition and the irregular time-dependent geometry of a melting front precludes a meaningful set of scales. Moreover, the additional dependence of the transport mechanism on the local melt fraction and the strongly variable viscosity considered here significantly increases the scaling complexity. However, a scaling investigation is unnecessary to demonstrate the influence of complex melting relations on the dynamics of melt movement and the progress of melting.

For the purpose of normalizing the results, we assume that the total duration of the simulations (approximately 160 years) reflects a reasonable characteristic time over which a constant temperature contact may be maintained in analogous geological systems. The perturbation period thus provides a useful timescale with which to generalize the results. We acknowledge the ad hoc nature of this choice of scales. However, there is some geological justification for using the stated period as a basis for characteristic scales. A horizontal intrusion (sill) of mafic magma beneath a sequence of metasedimentary rocks is thought to have a role in the generation of some igneous rocks [15]. This configuration is also analogous to the system under consideration in this study. A simple calculation shows that the total enthalpy absorbed by the one-invariant-point model would require the heat released from the cooling and solidification of an underlying sill of mafic magma that was approximately 100 m thick. This sill thickness has been shown to be characteristic in several important geological systems, including those resembling that under consideration here [22, 23]. Accordingly, we define the nondimensional time to be

$$t^* = \frac{t}{t_f} \tag{9}$$

where t_f is the total time duration of the simulations (5×10^9 s).

The thermal and dynamical state of the one- and two-invariant-point systems at $t^* = 0.2$ is shown in Figures 6*a* and 6*b*, respectively. The progression of the style of convection was similar in both cases. Convection was initially characterized by numerous small convection cells over the heated strip. The wavelength of the initial instabilities as defined by the separation of the upwellings was approximately 20–25 m. As the cavity aspect ratio grew, certain cells grew at the expense of others until convection was dominated by a single counterclockwise rotating convection cell.

The temporal evolution of convective style proceeded much more rapidly in the two-invariant-point case. As a result, higher convective velocities, a more

Table 2. Values of various constants

Parameter	Value
Thermophysical and rheological properties	
Specific heat, J/(kg K)	1.04×10^3
Thermal conductivity, W/(m K)	1.9
Density, kg/m^3	2.507×10^3
Kinematic viscosity, m^2/s	see text
Schmidt number (μ^l/D)	1.0×10^6
Latent heat, J/kg	1.0×10^5
Permeability coefficient, m^2	5.56×10^{-10}
Thermal expansion coefficient, K^{-1}	1.05×10^{-4}
Solutal expansion coefficient	1.55×10^{-1}
Critical melt fraction	0.5
Initial and boundary conditions	
Pelite starting composition	0.325
Initial temperature, °C	600.0
Contact temperature, °C	1000.0
Total time duration of simulations, s	5×10^9
Phase diagram parameters (see also Table 1)	
*TM*1, °C	1250
*TM*2, °C	1600
Tq, °C	*Te*1 − ε
*Te*1, °C	700
*Te*2, °C	860
*Ce*1	0.873
*Ce*2	*kp*4 · *Clt*1
*Cps*1	0.1
*Cps*2	0.0
*kp*1	0.35
*kp*2	0.999
*kp*3	0.0001
*kp*4	0.999
ε, °C	10.0
Tt, °C	860

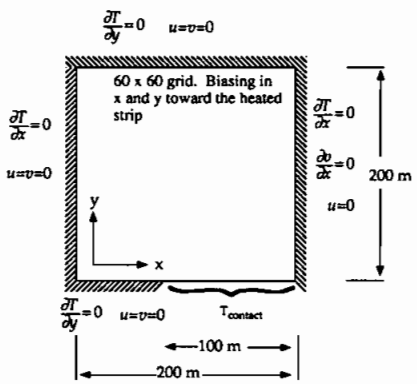

Figure 5. Schematic of computational domain.

rapidly propagating temperature perturbation, and more efficient melt generation were observed than in the one-invariant-point system. This is evident in Figure 6, where it can be seen that the height of the convecting cavity (defined by the CMF) in the two-invariant-point case (Figure 6*b*) had propagated nearly 3 times farther than in the one-invariant-point case (Figure 6*a*). In addition, convection in the two-invariant-point case is fully developed (i.e., a single counterclockwise rotating cell) at the selected time, whereas five convection cells are still evident in the single-invariant-point case.

The enhanced convection in the two-invariant-point system resulted from the fact that more melt was generated at lower temperatures. Owing to the elevated low-temperature melt productivity, the two-invariant-point system exceeded the CMF approximately 100°C lower in temperature than the one-invariant-point case (Figure 4). Bulk viscous flow of the mixture consequently occurred earlier in the course of the simulations and was more vigorous in the two-invariant-point case. Since the buoyant porous flow of melt is an inefficient mechanism for transporting heat in this system [6], any reduction in convective vigor of the mixture may have a substantial impact on heat transport and the progress of melting.

The increase in convective vigor concomitant with the increase in melt productivity is further illustrated in Figures 7 and 8. Figure 7 depicts the evolution of the flux ratio (ϑ) as a function of time in the one- and two-invariant-point systems. We define ϑ as the ratio of the transient instantaneous average heat flux across the heated strip measured in a convection simulation relative to that

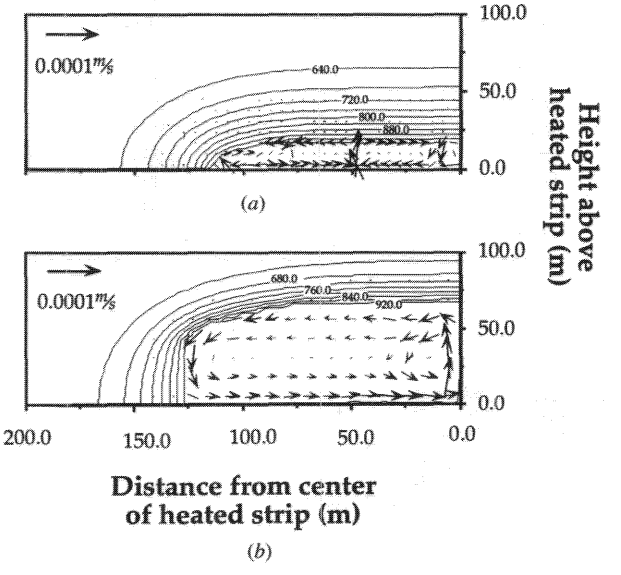

Figure 6. The mixture velocity (arrows) and temperature (contours in °C) of the two models at $t^* = 0.2$: (*a*) one- and (*b*) two-invariant-point system, respectively. The CMF ($f^l = 0.5$) approximately bounds the limits of significant convection in both plots.

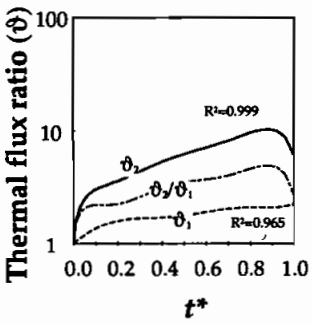

Figure 7. Plot of the flux ratio (ϑ). Subscripts indicate the one- and two-invariant-point simulation results. R^2 values on the chart indicate the statistical goodness-of-fit of the curves to the data. Variability in the data is attributed to time-dependent irregularities in the growth of the solidus front. The decay in ϑ at $t^* \approx 0.9$ results from the decrease in the temperature gradient due to sidewall heating.

predicted by conduction alone. The ϑ is thus analogous to the Nusselt number (Nu), which is often used to characterize the efficiency of convection for steady state convective heat transport problems. The variability in the instantaneous heat flux in the convection simulations resulted in some scatter in ϑ. This observation is consistent with other experiments and simulations where such irregularities have been attributed to the unsystematic time-dependent nature of the solidus front growth rate [2]. Accordingly, the plots in Figures 7 and 8 are best fits to the measured data. Statistical data regarding the goodness of fit are provided with the figures.

At $t^* = 0.2$, coincident with the example simulation shown in Figure 6, $\vartheta = 3.625$ in the two-invariant-point case. At the same time, $\vartheta = 1.603$ in the one-invariant-point case. The efficiency of convective heat transport, as measured by ϑ, was elevated by approximately 225% owing to the enhanced low-temperature melt productivity in the two-invariant-point case. The increased efficiency is also illustrated by the ratio of ϑ in the two-invariant-point case to that of the one-invariant-point case (ϑ_2/ϑ_1), depicted in Figure 7. The ratio ϑ_2/ϑ_1 grows to a high of 4.962 at $t^* = 0.88$, then begins to decay. The decay in ϑ beginning at $t^* = 0.9$ was due to thermal interaction of the temperature perturbation with the insulated walls. The simulations indicate that heat transport between the two systems will continuously diverge until the temperature gradient begins to decrease, when the temperature perturbation preceding the convective upwelling reaches the roof of the computational domain.

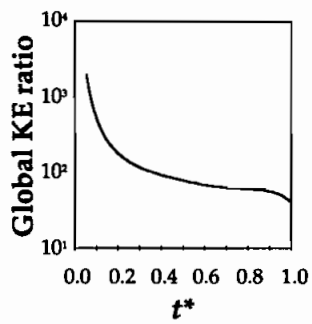

Figure 8. Plot of the ratio of the global kinetic energy (KE) of the two-invariant-point system to that of the one-invariant-point system. High values at low t^* indicate that convection in the two-invariant-point case initiated earlier than in the one-invariant-point case. Increasing decay at $t^* \approx 0.9$ is due to sidewall heating in the two-invariant-point case.

Numerous experiments of natural convection in enclosures have been conducted that have resulted in several empirical equations relating the steady state thermal Rayleigh number (Ra_t) to an instantaneous average Nu. The experiments most relevant to the present study are those of Chu and Hickox [24], who considered natural convection with strongly variable viscosity and an analogous geometry. Chu and Hickox [24] observe that

$$Nu_m = 0.54(Ra_m)^{0.25}\left(\frac{\mu_o}{\mu_h}\right)^{-0.035} \tag{10}$$

where the subscripts m, o, and h indicate that the properties are measured at the mean, upper surface, or heated strip temperatures, respectively. It is a simple matter to ignore density change as a function of composition, calculate Ra_t, and use the empirical relation given in Eq. (10) to predict Nu. However, such calculations yield a value of Nu that is approximately an order of magnitude higher than the observed ϑ. The major differences between the systems are the latent heat exchange and the buoyancy resulting from compositional gradients. We observed that the compositional Ra (Ra_c) was the same order of magnitude as Ra_t and that the density variation resulting from the composition gradient was opposite to that of the temperature gradient. To test the influence of double-diffusive effects, we conducted a series of simulations in which Ra_c was set to zero. In this analysis, ϑ was found to closely correspond with Nu obtained from Eq. (10) despite the various differences between the studies. We conclude that, in this system, double-diffusive convection gives rise to more sluggish heat transfer than would be expected from an analysis based on the temperature gradients alone.

Figure 8 illustrates the relative difference in the increase in the global kinetic energy (KE). The global KE was defined as

$$\sum \mathrm{KE}_i = \tfrac{1}{2}\rho V_i(v_i^2 + u_i^2) \tag{11}$$

where V_i, v_i, and u_i indicate the partial volume, vertical velocity, and horizontal velocity of the ith control volume, respectively. The global KE was calculated by summing the KE for the control volumes over the computational domain. The data in Figure 8 were obtained by taking the ratio of the global KE for the two-invariant-point case to that of the one-invariant-point case. The KE ratio decayed from an initial high value of approximately 10^4 at $t^* = 0.05$ exponentially, approaching a value of approximately 10^2 asymptotically. At $t^* = 0.9$ the KE ratio began to decay again, corresponding with the decay in ϑ previously discussed. The high initial values of the KE ratio at low t^* are attributed to the two-invariant-point system initiating convection earlier than in the one-invariant-point case. The asymptotic decay to a value exceeding 1 indicates that, all else being equal, convective vigor in the two-invariant-point system will always exceed that of the one-invariant-point case.

CONCLUSIONS

A new phase diagram has been developed in order to evaluate the influence of melt productivity in complex systems undergoing phase change. The new phase diagram features two invariant points—a eutectic and a peritectic—and was used in a series of two-dimensional simulations of melting with variable viscosity. The results of these simulations were compared with those obtained from another series that used a one-invariant-point phase-change model. The solidus front was observed to propagate away from the heated contact much more rapidly in the two-invariant-point case. For example, at $t^* = 0.2$ the solidus front had propagated over 3 times farther. Additionally, the efficiency of convective heat transport and the global kinetic energy were found to be greater by over 200% and 2 orders of magnitude, respectively. This comparison demonstrates that the complementary relation between melt productivity and the rheology of partially molten systems may have a large impact on the progress of melting and vigor of convection. The two-invariant-point phase diagram permits the extension of the continuum mixture formulation to systems with more complex melt productivity, where such coupling may be significant.

REFERENCES

1. W. D. Bennon and F. P. Incropera, A Continuum Model for Momentum, Heat and Species Transport in Binary Solid-Liquid Phase Change Systems, I: Model Formulation, *Int. J. Heat Mass Transfer*, vol. 30, pp. 2161–2170, 1987.
2. W. D. Bennon and F. P. Incropera, A Continuum Model for Momentum, Heat and Species Transport in Binary Solid-Liquid Phase Change Systems, II: Application to Solidification in a Rectangular Cavity, *Int. J. Heat Mass Transfer*, vol. 30, pp. 2171–2187, 1987.
3. C. Prakash and V. R. Voller, On the Numerical Solution of Continuum Mixture Model Equations Describing Binary Solid-Liquid Phase Change, *Numer. Heat Transfer Part B*, vol. 15, pp. 171–189, 1989.
4. C. M. Oldenburg and F. J. Spera, Hybrid Model for Solidification and Convection, *Numer. Heat Transfer Part B*, vol. 21, pp. 217–229, 1992.
5. D. Vielzeuf and J. R. Holloway, Experimental Determination of the Fluid-Absent Melting Relations in the Pelitic System, *Contrib. Mineral. Petrol.*, vol. 98, pp. 257–276, 1988.
6. S. A. Barboza and G. W. Bergantz, Dynamic Model of Dehydration Melting Motivated by a Natural Analogue: Applications to the Ivrea-Verbano Zone, Northern Italy, *Trans. R. Soc. Edinburgh*, vol. 87, pp. 23–31, 1996.
7. C. Beckermann and R. Viskanta, Mathematical Modeling of Transport Phenomenas During Alloy Solidification, *Appl. Mech. Rev.*, vol. 46, pp. 1–27, 1993.
8. B. D. Marsh, On the Crystallinity, Probability of Occurrence, and Rheology of Lava and Magma, *Contrib. Mineral. Petrol.*, vol. 78, pp. 85–98, 1981.
9. C. F. Miller, E. B. Watson, and T. M. Harrison, Perspectives on the Source, Segregation and Transport of Granitoid Magmas, *Trans. R. Soc. Edinburgh: Earth Sciences*, vol. 79, pp. 135–156, 1988.
10. T. Rushmer, An Experimental Deformation Study of Partially Molten Amphibolite: Application to Low-Melt Fraction Segregation, *J. Geophys. Res.*, vol. 100, pp. 15681–15695, 1995.

11. E. H. Rutter and D. H. K. Neumann, Experimental Deformation of Partially Molten Westerly Granite Under Fluid-Absent Conditions, with Implications for the Extraction of Granitic Magmas, *J. Geophys. Res.*, vol. 100, pp. 15697–15715, 1995.
12. C. Beckermann and R. Viskanta, Double-Diffusive Convection During Dendritic Solidification of a Binary Mixture, *Physiochem. Hydrodyn.*, vol. 10, pp. 195–213, 1988.
13. H. R. Shaw, Viscosities of Magmatic Liquids: An Empirical Method of Prediction, *Am. J. Sci.*, vol. 272, pp. 870–893, 1972.
14. C. R. Wildemuth and M. C. Williams, Viscosity of Suspensions Modeled with a Shear-Dependent Maximum Packing Fraction, *Rheol. Acta*, vol. 23, pp. 627–635, 1984.
15. G. W. Bergantz and R. Dawes, Aspects of Magma Generation and Ascent in Continental Lithosphere, in M. P. Ryan (ed.), *Magmatic Systems*, pp. 291–317, Academic Press, San Diego, Calif., 1994.
16. A. E. Patiño Douce and A. D. Johnston, Phase Equilibria and Melt Productivity in the Pelitic System: Implications for the Origin of Peraluminous Granitoids and Aluminous Granulites, *Contrib. Mineral. Petrol.*, vol. 107, pp. 202–218, 1990.
17. N. Le Breton and A. B. Thompson, Fluid-Absent (Dehydration) Melting of Biotite in Metapelites in the Early Stages of Crustal Anatexis, *Contrib. Mineral. Petrol.*, vol. 99, pp. 226–237, 1988.
18. S. A. Barboza, The Dynamics of Dehydration Melting and Implications for Melt Extraction in the Lower Crust Following Underplating: An Example from the Ivrea-Verbano Zone, Northern Italy, M.S. thesis, University of Washington, Seattle, 1995.
19. S. V. Patankar, *Numerical Heat Transfer and Fluid Flow*, 197 pp., Hemisphere, New York, 1980.
20. H. I. Rosten and D. B. Spalding, The PHOENICS Reference Manual, CHAM TR/200, 1987.
21. C. M. Oldenburg and F. J. Spera, Numerical Modeling of Solidification and Convection in a Viscous Pure Binary Eutectic System, *Int. J. Heat Mass Transfer*, vol. 34, pp. 2107–2121, 1991.
22. J. M. Sinton and R. S. Detrick, Mid-Ocean Ridge Magma Chambers, *J. Geophys. Res.*, vol. 97, pp. 197–216, 1992.
23. J. E. Quick, S. Sinigoi, and A. Mayer, Emplacement Dynamics of a Large Mafic Intrusion in the Lower Crust of the Ivrea-Verbano Zone, Northern Italy, *J. Geophys. Res.*, vol. 99, pp. 21559–21573, 1994.
24. T. Y. Chu and C. E. Hickox, Thermal Convection with Large Viscosity Variation in an Enclosure with Localized Heating, *J. Heat Transfer*, vol. 112, pp. 388–395, 1990.